cell fate decision. We suggest that identifying such prepatterns in other progenitors could help to predict lineage-specific developmental potential. Such information from native embryonic cells can be used to define benchmarks of proper progenitor cell programming from stem cells. In addition, the relevant chromatin-modifying enzymes can serve as pharmacologic targets to enhance particular cell fate transitions from stem cells, as we did with P300 from native endoderm.

References and Notes

1. B. E. Bernstein *et al.*, *Cell* **125**, 315 (2006).
2. A. Rada-Iglesias *et al.*, *Nature* **470**, 279 (2011).
3. J. Xu *et al.*, *Genes Dev.* **23**, 2824 (2009).
4. J. A. Dahl, P. Collas, *Nat. Protoc.* **3**, 1032 (2008).
5. G. Deutsch, J. Jung, M. Zheng, J. Lóra, K. S. Zaret, *Development* **128**, 871 (2001).
6. R. Bort, J. P. Martinez-Barbera, R. S. Beddington, K. S. Zaret, *Development* **131**, 797 (2004).
7. K. S. Zaret, *Nat. Rev. Genet.* **9**, 329 (2008).
8. P. Gadue *et al.*, *Stem Cells* **27**, 2103 (2009).
9. R. Gualdi *et al.*, *Genes Dev.* **10**, 1670 (1996).
10. T. Watanabe *et al.*, *Dev. Biol.* **250**, 332 (2002).
11. K. Gorski, M. Carneiro, U. Schibler, *Cell* **47**, 767 (1986).
12. J. K. Liu, C. M. DiPersio, K. S. Zaret, *Mol. Cell. Biol.* **11**, 773 (1991).
13. M. H. Feuerman, R. Godbout, R. S. Ingram, S. M. Tilghman, *Mol. Cell. Biol.* **9**, 4204 (1989).
14. R. H. Costa, D. R. Grayson, J. E. Darnell Jr., *Mol. Cell. Biol.* **9**, 1415 (1989).
15. D. F. Boyer *et al.*, *Dev. Biol.* **298**, 616 (2006).
16. N. Gao *et al.*, *Genes Dev.* **22**, 3435 (2008).
17. K. Gerrish, J. C. Van Velkinburgh, R. Stein, *Mol. Endocrinol.* **18**, 533 (2004).
18. S. Y. Roth, J. M. Denu, C. D. Allis, *Annu. Rev. Biochem.* **70**, 81 (2001).
19. J. A. Simon, R. E. Kingston, *Nat. Rev. Mol. Cell Biol.* **10**, 697 (2009).
20. L. Qiao, J. Shao, *J. Biol. Chem.* **281**, 39915 (2006).
21. F. Seydel *et al.*, *J. Autoimmun.* **31**, 377 (2008).
22. W. Xu *et al.*, *Nat. Genet.* **26**, 229 (2000).
23. T. P. Yao *et al.*, *Cell* **93**, 361 (1998).
24. T. Yamauchi *et al.*, *Proc. Natl. Acad. Sci. U.S.A.* **97**, 11303 (2000).
25. W. Lin *et al.*, *Dev. Dyn.* **237**, 928 (2008).
26. R. L. Schiltz *et al.*, *J. Biol. Chem.* **274**, 1189 (1999).
27. T. Kouzarides, *Cell* **128**, 693 (2007).
28. E. Wandzioch, K. S. Zaret, *Science* **324**, 1707 (2009).
29. E. M. Bowers *et al.*, *Chem. Biol.* **17**, 471 (2010).
30. R. Cao *et al.*, *Science* **298**, 1039 (2002).
31. I. H. Su *et al.*, *Nat. Immunol.* **4**, 124 (2003).
32. C. S. Lee, J. R. Friedman, J. T. Fulmer, K. H. Kaestner, *Nature* **435**, 944 (2005).
33. C. Pouponnot, L. Jayaraman, J. Massagué, *J. Biol. Chem.* **273**, 22865 (1998).
34. M. P. de Caestecker *et al.*, *J. Biol. Chem.* **275**, 2115 (2000).
35. G. C. Chu, N. R. Dunn, D. C. Anderson, L. Oxburgh, E. J. Robertson, *Development* **131**, 3501 (2004).
36. J. van Arensbergen *et al.*, *Genome Res.* **20**, 722 (2010).
37. V. Azuara *et al.*, *Nat. Cell Biol.* **8**, 532 (2006).

Acknowledgments: We thank T. Jiang, R. Hardy, J. Oesterling, and W. DeMuth for assistance; Z. Zhang, J. Xu, and S. Hua for advice; P. Streeter and K. Kaestner for reagents; J. Epstein, E. Wandzioch, D. Metzger, A. Wecker, A. Hines, and D. Freedman-Cass for comments; and E. Pytko for preparing the manuscript. Supported by the FAMRI Foundation and NIH grant U54MH084691 (P.A.C. and D.J.M.), NIH grant RO1 GM067718 (S.D.), and NIH grants R37GM36477 and U01DK072503 (K.S.Z.). There is a patent on P300i: "Methods and compositions for modulating p300/CBP activity" (pub. WO/2008/157680; international application PCT/US2008/067477 to D.J.M. and P.A.C.). P.A.C. is co-founder, owns equity, and receives consulting fees as science advisor to Acylin Therapeutics, which is attempting the development of clinically useful HAT inhibitors and licenses from Johns Hopkins some of our discoveries related to C646.

Supporting Online Material

www.sciencemag.org/cgi/content/full/332/6032/963/DC1
Materials and Methods
Figs. S1 to S12
Tables S1 to S3
References

13 January 2011; accepted 8 April 2011
10.1126/science.1202845

Spatial Coupling of mTOR and Autophagy Augments Secretory Phenotypes

Masako Narita,[1]* Andrew R. J. Young,[1]* Satoko Arakawa,[2] Shamith A. Samarajiwa,[1,3] Takayuki Nakashima,[1]† Sei Yoshida,[4] Sungki Hong,[4] Lorraine S. Berry,[1] Stefanie Reichelt,[1] Manuela Ferreira,[1]‡ Simon Tavaré,[1,3] Ken Inoki,[4] Shigeomi Shimizu,[2] Masashi Narita[1]§

Protein synthesis and autophagic degradation are regulated in an opposite manner by mammalian target of rapamycin (mTOR), whereas under certain conditions it would be beneficial if they occurred in unison to handle rapid protein turnover. We observed a distinct cellular compartment at the trans side of the Golgi apparatus, the TOR-autophagy spatial coupling compartment (TASCC), where (auto)lysosomes and mTOR accumulated during Ras-induced senescence. mTOR recruitment to the TASCC was amino acid– and Rag guanosine triphosphatase–dependent, and disruption of mTOR localization to the TASCC suppressed interleukin-6/8 synthesis. TASCC formation was observed during macrophage differentiation and in glomerular podocytes; both displayed increased protein secretion. The spatial coupling of cells' catabolic and anabolic machinery could augment their respective functions and facilitate the mass synthesis of secretory proteins.

During oncogene-induced senescence (OIS), a dynamic transition in phenotype is mediated by multiple effector mechanisms, including the secretory phenotype (*1*, *2*) and autophagy (*3*). Senescent cells continue to grow in size and produce large amounts of secretory proteins; therefore, protein synthesis also seems to be activated. The active protein turnover caused by coupling protein degradation and synthesis may facilitate acute phenotypic regeneration. To understand how these processes are coregulated during OIS, we examined the spatial relation between mammalian target of rapamycin (mTOR) (*4*, *5*) and autophagy (*6*, *7*) in IMR90 cells stably expressing 4-hydroxytamoxifen (4OHT)–inducible H-*Ras*V12 (ER:Ras) (*3*, *8*).

Autophagy markers, p62 and LC3, formed prominent puncta and colocalized throughout the cytoplasm upon amino acid (AA) starvation in IMR90 cells, whereas growing cells only formed occasional puncta (Fig. 1A) (*9*–*11*). In contrast, during Ras-induced senescence (RIS), cells exhibited distinct cytoplasmic areas that were enriched for p62 and LC3 (Fig. 1A). This autophagic area overlapped with senescence-associated–β-galactosidase activity (a lysosomal enzyme) and LAMP2 (a lysosomal protein), suggesting autolysosome enrichment (Fig. 1A and fig. S1, A and B). Locally concentrated p62 can form detergent-insoluble aggresomes. However, they typically do not colocalize to lysosomes (*11*, *12*), and there was no increase in p62 or LC3 in the Triton X-insoluble fraction during RIS (Fig. 1B), indicating active autophagy (fig. S1C).

We next determined the subcellular localization of mTOR, which also congregated in distinct cytoplasmic areas in RIS cells, but not in growing cells (Fig. 1C). The mTOR-, LAMP2-, and p62-positive areas overlapped (Fig. 1, C and D, and fig. S1D). Furthermore, the mTOR and LAMP2 signals were spatially associated with each other more frequently inside than outside these areas (fig. S2). Thus, protein degradation and synthesis may be spatially coupled during RIS in an area we call the TOR-autophagy spatial coupling compartment (TASCC).

mTOR complex 1 (mTORC1) negatively regulates autophagy upstream of the Atg1/ULK complex, which plays an essential role at the early stage of autophagosome formation (*13*, *14*). To test whether autophagosomes are formed outside the TASCC and then move into the TASCC to form autolysosomes, we examined the location of ULK1 and ATG12, which only localize transiently to developing autophagosomes (*15*–*17*). The developing autophagosomes containing

[1]Cancer Research UK Cambridge Research Institute (CRI), Li Ka Shing Centre, Robinson Way, Cambridge CB2 0RE, UK. [2]Department of Pathological Cell Biology, Medical Research Institute, Tokyo Medical and Dental University, 1-5-45 Yushima, Bunkyo-ku, Tokyo 113-8510, Japan. [3]Department of Oncology, University of Cambridge, Cambridge CB2 0RE, UK. [4]Life Sciences Institute, Department of Molecular and Integrative Physiology and Internal Medicine, University of Michigan, 210 Washtenaw Avenue, Ann Arbor, MI 48109, USA.

*These authors contributed equally to this work.
†Present address: Kyowa Hakko Kirin, Shizuoka 411-8731, Japan.
‡Present address: Instituto de Medicina Molecular, Faculdade de Medicina de Lisboa, 1649-028 Lisbon, Portugal.
§To whom correspondence should be addressed. E-mail: masashi.narita@cancer.org.uk

ULK1/ATG12 were indeed excluded from the TASCC (Fig. 1E, fig. S3, and movie S1). In addition, we used tandem monomeric red fluorescent protein–green fluorescent protein (mRFP-GFP)–LC3, in which GFP is more sensitive to acidic conditions than mRFP. Thus, both signals are active in autophagosomes, but the mRFP signal is predominant in autolysosomes (*10*, *18*). The TASCC was mostly occupied by autolysosomes with a prominent red signal, whereas mixed signals from green and red were found in the isolated puncta surrounding the TASCC (fig. S4). Spatial organization of mTOR and developing autophagosomes may thus allow their simultaneous activation.

Electron microscopy (EM) analysis also revealed a distinctive cytoplasmic compartmentalization in RIS cells, with prominent autophagic vacuoles (Fig. 2, A to E). Well-developed Golgi apparatus (GA) and vesicles were enriched around these compartments and rough endoplasmic reticulum (rER) was often found adjacent to them, suggesting that high levels of protein synthesis take place around them (fig. S5). Confocal images showed that the trans-Golgi network (TGN), which typically exhibited a perinuclear pattern in growing cells, was mostly positioned close to the TASCC (fig. S6). Fluorescence-EM imaging confirmed the spatial relation between the GA, rER, and TASCC (Fig. 2, B to E, and fig. S7). The TASCC-GA association was recapitulated in mouse papillomas, an in vivo OIS model (fig. S8).

Lysosomal, membrane, and secretory proteins newly synthesized at the rER are processed within the GA and sorted into the TGN. To directly visualize this process, we performed metabolic labeling using a Click-iT (Invitrogen, Carlsbad, CA) methionine analog, L-homopropargylglycine (HPG), which allows us to detect nascent proteins by fluorescence (fig. S9). A 30-min pulse of HPG in RIS cells resulted in a cytoplasmic distribution of the nascent proteins, which were excluded from the TASCC but enriched in the TGN (Fig. 2F). After a 90-min chase with normal medium, labeled proteins were readily detected in the TASCC, confirming that proteins actively processed through the rER-GA were enriched in the TASCC (Fig. 2G). Consistently, interleukins 6 and 8 (IL-6/8), senescence-associated secretory proteins, were enriched in the TGN and/or TASCC in RIS cells (fig. S6). After shorter labeling (3 min), nascent proteins were often enriched in the area close to the TASCC (Fig. 2H and fig. S9D). The labeled proteins did not yet overlap with the TGN; thus, the signal is likely to represent sites of protein synthesis. Similarly, *IL-8* mRNA was detected at the marginal regions of the TASCC, particularly during the early phase of RIS (fig. S10).

To further characterize the TASCC, we asked whether the microtubule depolymerizing drug nocodazole affects TASCC formation (fig. S11). The TASCC was intact after 2 hours of treatment on day 4, suggesting that microtubules were not required for TASCC maintenance (Fig. 3A). Similarly, nocodazole did not prevent TASCC induction when added upon Ras induction and subsequently for 24 hours (Fig. 3B). Nocodazole fragments GA, causing "mini-stacks," which are functionally active (*19*). The spatial relation between the TASCC and the mini-stacks was preserved (Fig. 3, C and D), reinforcing the importance of the process of protein transfer through the rER-GA-TASCC. We next assessed the requirement for a functional rER-GA system for TASCC formation using brefeldin A (BFA), which effectively blocks protein transport from the ER to the GA. BFA did not affect TASCC maintenance, but it did prevent TASCC formation (Fig. 3B and fig. S11). Importantly, basal non-TASCC lysosomes were intact (Fig. 3E), suggesting that de novo lysosome biogenesis is critical for TASCC induction. Functional Gene Ontology analysis of day 4 expression microarray data revealed significant enrichment for genes involved in membrane biogenesis, including lysosomes, GA, and ER (fig. S12 and table S1). Thus, activated lysosomal and membrane biogenesis may contribute to TASCC formation in the vicinity of the TGN, where secretory proteins are also processed.

The Rag/Gtr family of small guanosine triphosphatases (GTPases) mediate AA signaling to TORC1 (*20*, *21*). In mammalian cells, in response to AAs, the Rag GTPase complex recruits mTORC1 to lysosomes, where mTOR is activated by Rheb (*20*, *22*). Dominant negative (DN) forms of Rag GTPases can disrupt the AA-mediated mTORC1-lysosome association (*20*–*22*). We tested whether Rag GTPases are involved in TASCC-formation. RagB/C were enriched in the TASCC (fig. S13A). When *RagB*-DN was stably expressed in ER:Ras cells (fig. S13B), there was no obvious effect on LAMP2 enrichment at day 4 (Fig. 4A), nor on total mTOR levels (fig. S13C). However, mTOR enrichment in this area was significantly suppressed (Fig. 4A). The induction of IL-6/8 during RIS was substantially inhibited posttranscriptionally, indicating a role for Rag GTPase–mediated mTOR-lysosome association in the TASCC (Fig. 4B and fig. S13D).

Because Rag GTPases are AA-specific TOR regulators, we asked whether AAs derived from (auto)lysosomes within the TASCC reinforce mTOR recruitment. We treated cells with inhibitors of lysosomal proteases [E64d and pepstatin

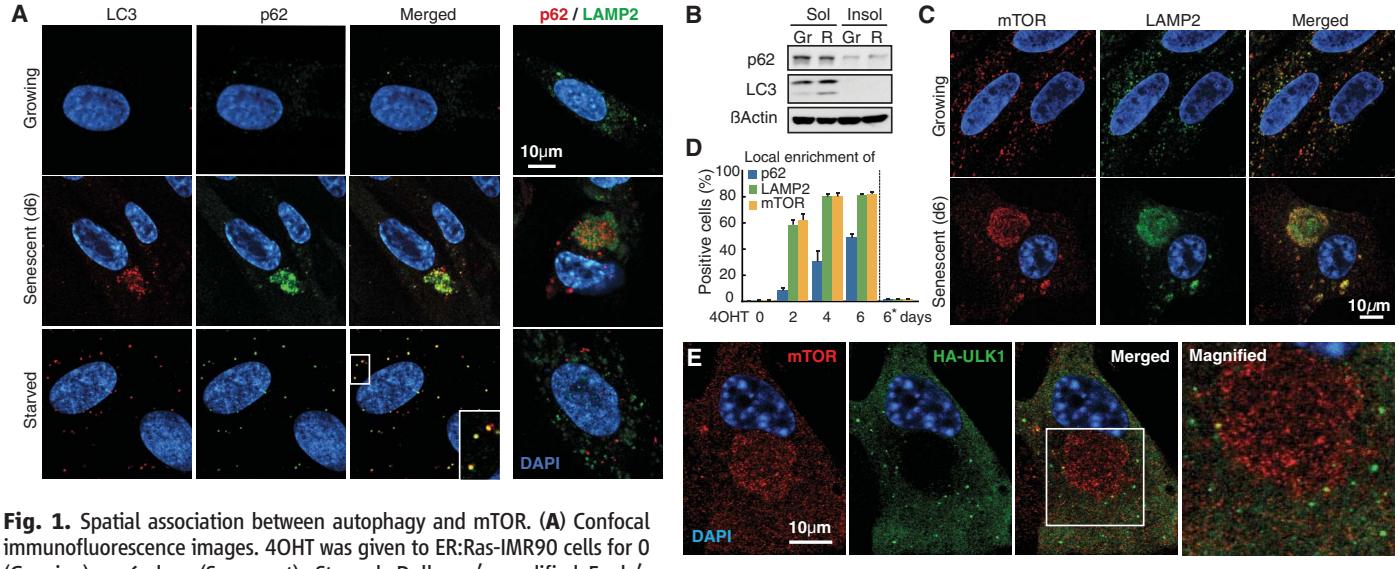

Fig. 1. Spatial association between autophagy and mTOR. (**A**) Confocal immunofluorescence images. 4OHT was given to ER:Ras-IMR90 cells for 0 (Growing) or 6 days (Senescent). Starved, Dulbecco's modified Eagle's medium without amino acids or serum for 2 hours. DAPI, 4′,6-diamidino-2-phenylindole. (**B**) Immunoblot analysis for indicated proteins in 1% Triton-X100 soluble (Sol) and insoluble (Insol) fractions from growing (Gr) and Ras-induced senescent (R) cells. (**C**) Confocal images of mTOR and LAMP2 immunofluorescence. (**D**) Quantification of TASCC-formation kinetics (mean ± SEM; $n \geq 3$ independent experiments). The asterisk indicates parental cells treated with 4OHT for 6 days. (**E**) Confocal images of mTOR and hemagglutinin (HA) immunofluorescence in HA-ULK1–expressing ER:Ras-IMR90 cells.

Fig. 2. Spatial association between TASCC and secretory apparatus. (**A**) EM of ER:Ras-IMR90 cells. 4OHT was given for 0 or 4 days. Arrows denote TASCC. Regions indicated by rectangles are magnified in fig. S5. (**B** to **E**) Fluorescence EM. LC3 (RFP) and Golgi (GFP) were BacMam system–labeled at day 4. Dashed lines represent grid on cover slip (B). Regions indicated by rectangles are magnified in corresponding figure panels (see also fig. S7). Blue arrows in (E) denote GA-derived coated vesicles. (**F** to **H**) Visualization of nascent protein synthesis during Ras-induced senescence (see fig. S9). After 30-min labeling with HPG in day 4 Ras-induced senescent cells (d4), nascent protein was accumulated in TGN (arrows), but not in the TASCC (F). After 90-min chase, nascent protein was readily detected in TASCC (arrows) (G). Short-term (3 min) labeling of HPG to visualize sites of protein synthesis (H).

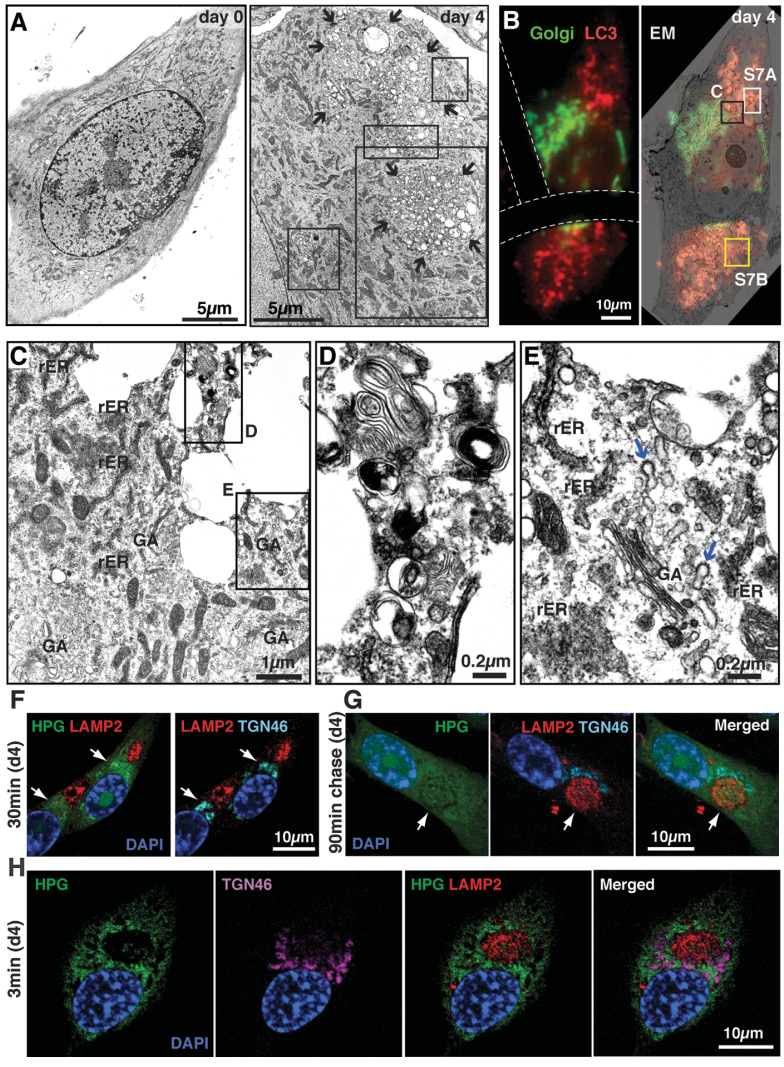

Fig. 3. BFA, but not nocodazole, prevents TASCC formation. (**A** and **B**) ER:Ras-IMR90 cells were treated with 10 μM nocodazole (NZ) or 40 ng/ml BFA, which were added after (A) or before (B) TASCC establishment. TASCC was assessed by mTOR/LAMP2 immunofluorescence. Error bars indicate SEM. (**C** to **E**) Representative confocal images of cells treated as in (B). RM130 and TGN46, cis- and trans-Golgi network markers, respectively.

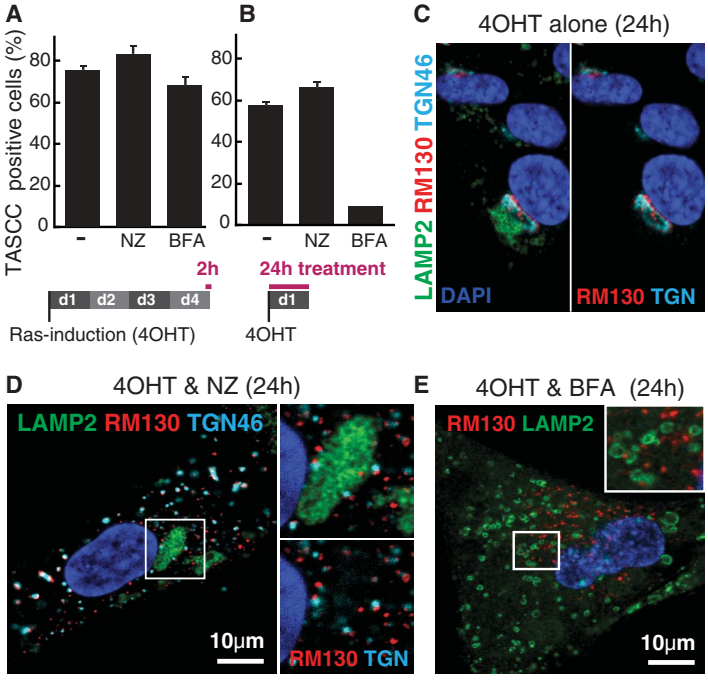

A (E&P)] and/or AA-free media (Fig. 4C). AA depletion showed no obvious effect on the local accumulation of LAMP2 in RIS cells. Three-hour treatment of day 4 ER:Ras cells with E&P or AA-free medium alone showed only marginal effects on mTOR accumulation in the TASCC. When E&P and AA-free medium were combined, enrichment of mTOR was significantly reduced, whereas enrichment of RagB, which constitutively localizes to lysosomes (*22*), was not reduced (Fig. 4C and fig. S14). The effect of adding E&P to the AA-free medium on mTOR dispersion was also significant, indicating a contribution of (auto)lysosome-derived AAs to mTOR recruitment at the TASCC (Fig. 4C). Similar results were obtained with ATG5 knockdown (fig. S15).

To identify the TASCC in different systems, we chose HL60 human promyelocytic leukemia cells, which can be differentiated into macrophage-like cells by 12-*O*-tetradecanoylphorbol-13-acetate (TPA) with transient up-regulation of *IL-8*. We found that this surge in IL-8 production was associated with the concomitant activation of autophagy (fig. S16, A to C). After TPA treatment, a substantial population of attached cells exhibited local enrichment for mTOR, RagB, lysosomes, and autophagy vacuoles at perinuclear regions, which were spatially associated with IL-8 and TGN, suggesting that the TASCC is also involved in macrophage differentiation (fig. S10C and fig. S16, D to F).

Looking for TASCC in a more physiological setting, we examined mouse renal glomerular podocytes, a core element of the filtration barrier in glomeruli. Podocytes, identified within regions facing capsule space in glomerulus sections (Fig. 4D), play a critical role in the constant turnover of glomerular basement membrane and endothelium maintenance by secreting vascular endothelial growth factor (VEGF) and many other factors. Podocytes exhibit an unusually high level of constitutive autophagy (*23*), suggesting simultaneous activation of anabolic and catabolic processes. We detected prominent GA, which were accompanied by enriched VEGF, mTOR, Lamp2, and LC3 (Fig. 4, E and F).

Recent reports have shown that AA re-addition induces Rag GTPase–dependent mTORC1-lysosome compartmentalization (*20*, *22*), and we now provide evidence for functional relevance for this process. We propose a model that may explain how cells can activate both protein synthesis and autophagic degradation (fig. S17). The spatial integration of rER-GA, autolysosomes, and mTOR creates a self-enhancing system, in which autolysosome-derived AAs reinforce mTOR enrichment and activity (*24*), leading to the efficient synthesis of secretory and lysosomal proteins (*5*). Furthermore, the TASCC might also function to sequester mTOR. Because the TASCC can be found in diverse contexts, it may represent a general mechanism for rapid protein turnover.

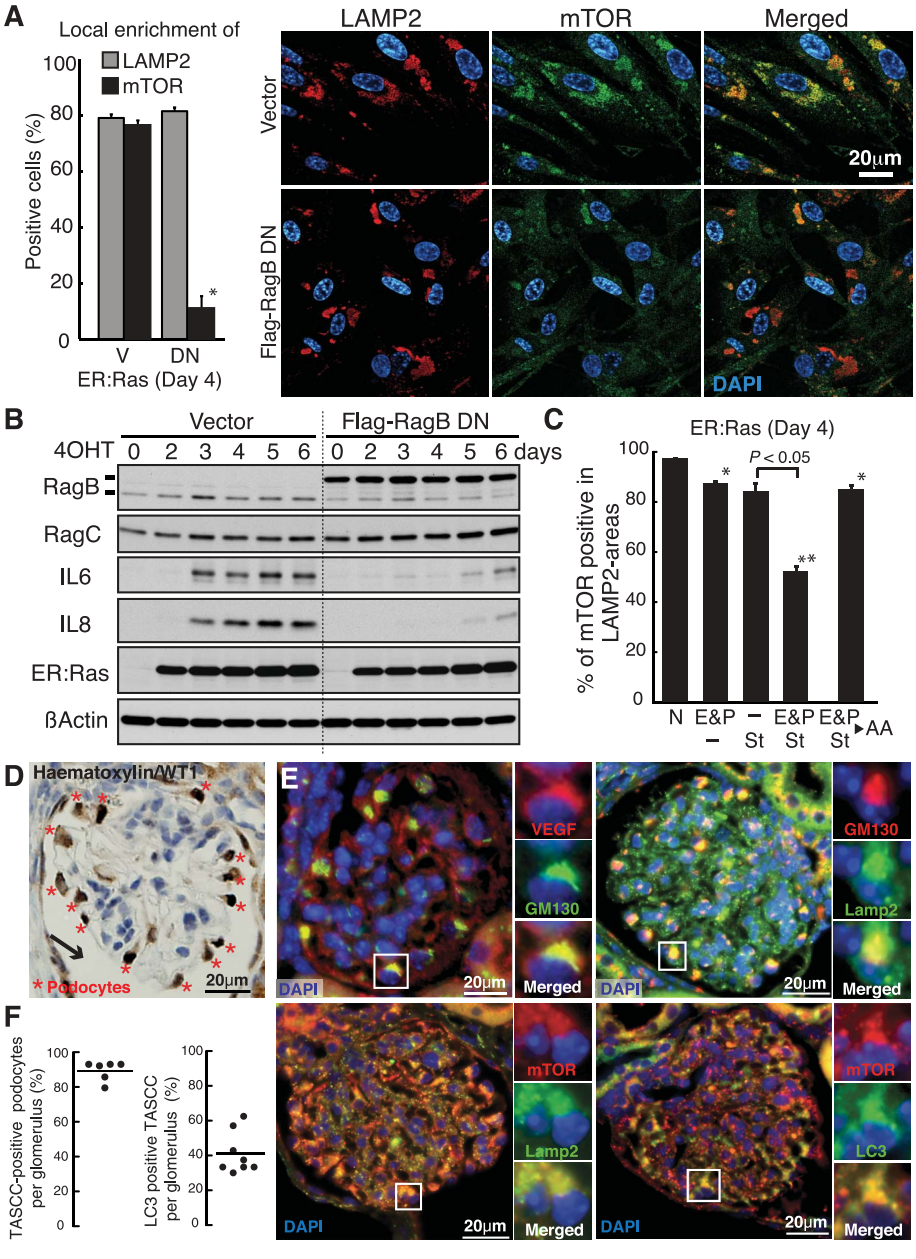

Fig. 4. Functional implication of TASCC. (**A** and **B**) ER:Ras-IMR90 cells expressing vector (V) or dominant negative mutant *RagB*-T54N (DN) were assessed for mTOR enrichment to LAMP2 compartments by immunofluorescence (mean ± SEM; $n = 3$) (A). $^{*}P < 0.01$ relative to V. Immunoblot analysis at time points indicated after Ras-induction (B). (**C**) Effect of AA depletion on mTOR enrichment in LAMP2 compartments as in (A). Cells were incubated with AA-free medium supplemented with 10% dialyzed fetal bovine serum (St) and/or lysosomal protease inhibitors [10 μg/ml E64d and 25 μg/ml pepstatin A (E&P)] for 3 hours. N, normal medium (fig. S14). As an additional control, we restored essential AAs (4AA) for 30 min after E&P/St treatment (mean ± SEM; $n = 3$). $^{*}P < 0.05$; $^{**}P < 0.01$ relative to N. (**D**) Typical immunohistochemical image of mouse glomerulus. WT1, podocyte marker; arrow, capsule space. (**E**) Representative images for indicated proteins in mouse glomeruli show TASCC in podocytes. (**F**) Percentages of TASCC-positive podocytes (left) and LC3 enrichment per TASCC-positive podocytes (right) in each glomerulus section were plotted. The black circles represent glomeruli sampled from two mice.

References and Notes

1. T. Kuilman, D. S. Peeper, *Nat. Rev. Cancer* **9**, 81 (2009).
2. J. P. Coppé, P. Y. Desprez, A. Krtolica, J. Campisi, *Annu. Rev. Pathol.* **5**, 99 (2010).
3. A. R. J. Young *et al.*, *Genes Dev.* **23**, 798 (2009).
4. S. Wullschleger, R. Loewith, M. N. Hall, *Cell* **124**, 471 (2006).
5. X. M. Ma, J. Blenis, *Nat. Rev. Mol. Cell Biol.* **10**, 307 (2009).
6. C. He, D. J. Klionsky, *Annu. Rev. Genet.* **43**, 67 (2009).
7. H. Nakatogawa, K. Suzuki, Y. Kamada, Y. Ohsumi, *Nat. Rev. Mol. Cell Biol.* **10**, 458 (2009).
8. Materials and methods are available as supporting material on *Science* Online.
9. Y. Kabeya *et al.*, *EMBO J.* **19**, 5720 (2000).
10. S. Pankiv *et al.*, *J. Biol. Chem.* **282**, 24131 (2007).
11. M. Komatsu *et al.*, *Cell* **131**, 1149 (2007).

12. J. A. Johnston, C. L. Ward, R. R. Kopito, *J. Cell Biol.* **143**, 1883 (1998).
13. N. Mizushima, *Curr. Opin. Cell Biol.* **22**, 132 (2010).
14. E. Y. Chan, S. Kir, S. A. Tooze, *J. Biol. Chem.* **282**, 25464 (2007).
15. T. Hara *et al.*, *J. Cell Biol.* **181**, 497 (2008).
16. C. H. Jung *et al.*, *Mol. Biol. Cell* **20**, 1992 (2009).
17. N. Mizushima, T. Yoshimori, B. Levine, *Cell* **140**, 313 (2010).
18. S. Kimura, T. Noda, T. Yoshimori, *Autophagy* **3**, 452 (2007).
19. J. Thyberg, S. Moskalewski, *Exp. Cell Res.* **246**, 263 (1999).
20. Y. Sancak *et al.*, *Science* **320**, 1496 (2008); 10.1126/science.1157535.
21. E. Kim, P. Goraksha-Hicks, L. Li, T. P. Neufeld, K.-L. Guan, *Nat. Cell Biol.* **10**, 935 (2008).
22. Y. Sancak *et al.*, *Cell* **141**, 290 (2010).
23. B. Hartleben *et al.*, *J. Clin. Invest.* **120**, 1084 (2010).
24. L. Yu *et al.*, *Nature* **465**, 942 (2010).

Acknowledgments: We thank K. Ryan, N. Mizushima, F. Watt, and R. Rios for reagents; R. Rios, D. Tuveson, T. Kanaseki, I. Mills, N. Dolman, and members of Narita lab for helpful discussion; L. Blackburn for editing; CRI's Genomics, Bioinformatics, Microscopy (J. Harris), and Histopathology facilities for technical support; and the Gurdon Institute's microscopy facility (A. Sossick) for optical microscopy experimental. This work was supported by the Univ. of Cambridge; Cancer Research UK; Hutchison Whampoa; Grants-in-Aid for Scientific Research from Ministry of Education, Culture, Sports, Science and Technology of Japan; the Program for Promotion of Fundamental Studies in the National Institute of Biomedical Innovation (S.A. and S.S.); and Juvenile Diabetes Research Foundation Award and NIH grant DK083491 (K.I.). Expression data are available at the National Center for Biotechnology Information Gene Expression Omnibus under accession number GSE28464.

Supporting Online Material

www.sciencemag.org/cgi/content/full/science.1205407/DC1
Materials and Methods
Figs. S1 to S17
Table S1
References
Movie S1

10 March 2011; accepted 11 April 2011
Published online 21 April 2011;
10.1126/science.1205407

Diet Drives Convergence in Gut Microbiome Functions Across Mammalian Phylogeny and Within Humans

Brian D. Muegge,[1] Justin Kuczynski,[2] Dan Knights,[3] Jose C. Clemente,[3] Antonio González,[3] Luigi Fontana,[4,5] Bernard Henrissat,[6] Rob Knight,[2,7] Jeffrey I. Gordon[1]*

Coevolution of mammals and their gut microbiota has profoundly affected their radiation into myriad habitats. We used shotgun sequencing of microbial community DNA and targeted sequencing of bacterial 16*S* ribosomal RNA genes to gain an understanding of how microbial communities adapt to extremes of diet. We sampled fecal DNA from 33 mammalian species and 18 humans who kept detailed diet records, and we found that the adaptation of the microbiota to diet is similar across different mammalian lineages. Functional repertoires of microbiome genes, such as those encoding carbohydrate-active enzymes and proteases, can be predicted from bacterial species assemblages. These results illustrate the value of characterizing vertebrate gut microbiomes to understand host evolutionary histories at a supraorganismal level.

Comparative culture-independent metagenomic studies of the microbial species assemblages that compose mammalian gut microbiota, and the functions that these communities encode in their aggregate genomes (microbiomes), can provide a complementary perspective to comparative studies of host genomes. A previous bacterial 16*S* ribosomal RNA (rRNA)–based study of 59 mammalian species revealed that their fecal microbiota clustered according to diet rather than host phylogeny (*1*). This finding raises several questions: What is the functional evolution of the gut microbiome in relation to diet? Is the process unique to each mammalian lineage? To what extent does microbial phylogeny predict function within microbial communities? Could analysis of interspecific differences among mammals create a pipeline for deciphering intraspecific differences among humans in response to varied diets or other factors? Therefore, we have extended our 16*S* rRNA studies to a broader sampling of microbial genes in total fecal community DNA prepared from herbivores, omnivores, and carnivores.

We generated shotgun pyrosequencing data sets from 33 mammalian species, along with newly collected bacterial 16*S* rRNA data. These adult animals represent 10 Orders and varied digestive physiologies (hindgut-fermenters, foregut-fermenters, and simple-gut). In some cases, free-living and captive representatives of a given species were sampled (Table 1 and table S1). Methods for classifying diets and for collecting and processing fecal samples for metagenomic analyses have been described (*1*). Multiplex pyrosequencing of amplicons generated from the V2 region of bacterial 16*S* rRNA genes yielded 149,675 high-quality de-noised reads (average = 3838 ± 1080 per sample) (table S2) (*2*). After chimera removal, 8541 operational taxonomic units (OTUs) were identified in the combined data set (an OTU was defined as reads sharing ≥97% nucleotide sequence identity). Shotgun sequencing of the same fecal DNA preparations produced 2,163,286 reads [mean = 55,469 ± 28,724 (SD) per sample; 261 ± 83 nt per read] (table S3) (*2*). Shotgun reads were functionally annotated using three databases: KEGG [for KEGG Orthology (KO) groups and Enzyme Commission (E.C.) numbers], CAZy (for carbohydrate-active enzymes), and MEROPS (for peptidases) (*3*–*5*). When shotgun reads were assigned to phylogenetic bins using the program MEGAN (*6*), the results revealed that fecal microbiomes were dominated by members of Bacteria, had low levels of Eukarya (0.15 to 5.35% of identifiable reads), and archaeons were variably represented (0 to 1.77% of assignable reads, with none detected in any carnivore microbiome). Seventeen samples had reads assigned to known viruses (table S4) (*2*).

Procrustes analysis (least-squares orthogonal mapping) was used to test whether the functional properties of a microbiome can be predicted from the bacterial species that compose it (*2*). Procrustes analysis attempts to stretch and rotate the points in one matrix, such as points obtained by principal coordinates analysis (PCoA), to be as close as possible to points in the other matrix, thus preserving the relative distances between points within each matrix (*7*, *8*) (Fig. 1A). We first took the 16*S* rRNA data set and used the UniFrac metric to compare the overlap between each pair of communities in terms of their evolutionary distance (*9*). The similarity in functional profiles was then determined using the Bray-Curtis distance metric applied to KO groups, E.C.s, CAZYmes, or peptidases. Principal-coordinates reduction was performed separately on the 16*S* rRNA and annotated shotgun (microbiome) data sets, and the point clouds were aligned using Procrustes. For each comparison, the goodness of fit, or M^2 value, of the transformed data sets was measured over the first three dimensions. The statistical significance of the goodness of the fit was measured by a Monte Carlo label permutation approach (*2*).

The agreement between phylogenetic and functional measurements was remarkable for all mammals, regardless of their diet, host lineage, or gut physiology. Figure 1, B to E, shows how the goodness of fit was robust to different functional databases. The analysis was also robust to taxon- or phylogenetic-based species classification, weighted or unweighted metrics, and whether one or more

[1]Center for Genome Sciences and Systems Biology, Washington University School of Medicine, St. Louis, MO 63108, USA. [2]Department of Molecular, Cellular and Developmental Biology, University of Colorado, Boulder, CO 80309, USA. [3]Department of Computer Science, University of Colorado, Boulder, CO 80309, USA. [4]Department of Medicine, Washington University School of Medicine, St. Louis, MO 63108, USA. [5]Division of Nutrition and Aging, Istituto Superiore di Sanità, Rome, Italy. [6]Architecture et Fonction des Macromolécules Biologiques, CNRS and Aix-Marseille Universities, Marseille, France. [7]Howard Hughes Medical Institute, Boulder, CO, USA.

*To whom correspondence should be addressed. E-mail: jgordon@wustl.edu